

**AN INTEGRATED FRAMEWORK FOR LIGHT CURVE
SIMULATION AND SHAPE INVERSION OF HUMAN-MADE
SPACE OBJECTS**

by

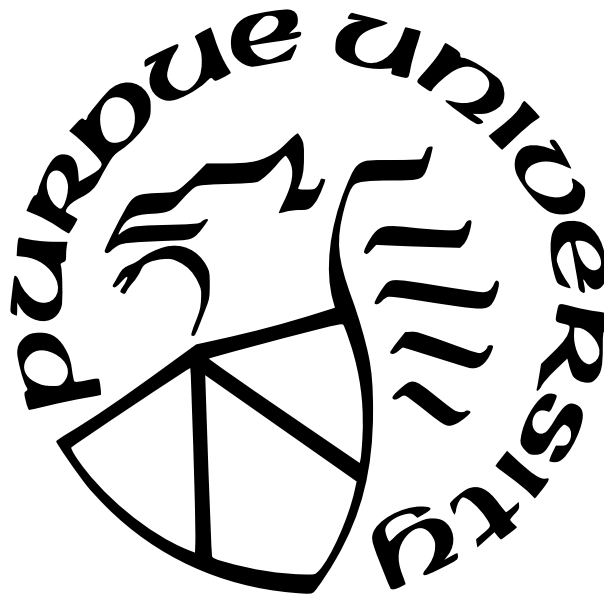
Liam Robinson

A Thesis

Submitted to the Faculty of Purdue University

In Partial Fulfillment of the Requirements for the degree of

Master of Science in Aeronautics and Astronautics



School of Aeronautics and Astronautics

West Lafayette, Indiana

December 2023

**THE PURDUE UNIVERSITY GRADUATE SCHOOL
STATEMENT OF COMMITTEE APPROVAL**

Dr. John Doe, Chair

School of Aeronautics and Astronautics

Dr. Jane Doe

School of Aeronautics and Astronautics

Dr. Jim Doe

School of Aeronautics and Astronautics

Approved by:

Dr. Buck Doe

To graduate students

ACKNOWLEDGMENTS

Purdue University's Engineering Computer Network and Graduate School helped fund PurdueThesis development.

PREFACE

This is the preface.

TABLE OF CONTENTS

LIST OF TABLES	8
LIST OF FIGURES	9
LIST OF LISTINGS	10
LIST OF SYMBOLS	11
ABSTRACT	12
1 Introduction	13
2 Literature	14
2.1 Coordinate Systems	17
2.1.1 International Terrestrial Reference Frame	17
2.1.2 Right Ascension and Declination	17
2.1.3 Azimuth and Elevation	17
3 MESHES	19
4 ATTITUDE REPRESENTATIONS	20
5 LIGHTING	23
6 Light Curves	25
6.1 Brightness Units	25
6.1.1 Irradiance	25
6.1.2 Normalized Irradiance	26
6.1.3 Candela	26
6.1.4 S_{10}	26
6.1.5 Magnitudes per Square Arcsecond	27
6.1.6 Photoelectron Counts	27
6.2 Astronomical Spectra	28

7	Background Signals	30
7.1	Atmospheric Effects	30
7.1.1	Airglow	30
7.1.2	Light Pollution	31
7.2	Exoatmospheric Effects	31
7.2.1	Integrated Starlight	31
7.2.2	Scattered Moonlight	34
7.2.3	Zodiacal Light	34
7.3	Sensor Effects	34
7.3.1	Dark Noise	34
7.3.2	Readout Noise	34
8	Light Curve Simulation	36
8.0.1	Simulating Convex Objects	36
9	Appendices	37
9.1	Astronomical Spectra Data	37
	Atmospheric Extinction	37
	Quantum Efficiency	37
9.1.1	Background Source Data	37
	Lunar Phase Factor	37
	Scattered Moonlight	38
	Zodiacal Light	39
	REFERENCES	40

LIST OF TABLES

LIST OF FIGURES

5.1	By default figures are not centered. This is a long caption to demonstrate that captions are single spaced. This is a long caption to demonstrate that captions are single spaced.	24
6.1	Astronomical Spectra	29
7.1	Airglow signal on the local observer hemisphere. The observer is in New Mexico, USA at 32.900° N, -105.533° W	31
7.2	Light pollution signal on the local observer hemisphere. The observer is in New Mexico, USA at 32.900° N, -105.533° W	32
7.3	Raw image of three GEO objects with stars streaking through the background. Taken by the Purdue Optical Ground station at 32.900° N, -105.533° W by Nathan Houtz	33
7.4	Integrated starlight patched catalog	34
7.5	Integrated starlight signal on the local observer hemisphere. The observer is in New Mexico, USA at 32.900° N, -105.533° W	35
7.6	Scattered moonlight signal on the local observer hemisphere. The observer is in New Mexico, USA at 32.900° N, -105.533° W	35

LIST OF LISTINGS

LIST OF SYMBOLS

I irradiance in $\left[\frac{W}{m^2}\right]$

\hat{I} normalized irradiance in $[W]$

ABSTRACT

PurdueThesis is a L^AT_EX document class used for master's bypass reports, master's theses, PhD dissertations, and PhD preliminary reports. This template demonstrates how to use PurdueThesis.

1. Introduction

This is the introduction

2. Literature

Light curve simulation methods differ between approaches and the object class under study. Kaasalainen and Torppa employ a Lambertian model for convex objects with a facetwise ray tracing scheme for non-convex objects [1]. Fan, Friedman, Kobayashi, and Frueh **freuh2014**, [2]–[5] use a nearly identical scheme for human-made objects. Allworth et al. developed a ray traced simulator for light curves in Blender, accounting for photorealistic shadowing and motion blur [6], [7]. Many deep learning approaches including Furfaro et al. [8] and Cabrera and Bradley [9], [10] use a simple Lambertian model with no self-shadowing. Linares and Crassidis **linares2017** apply a more specialized approach with a non-Lambertian Bidirectional Reflectance Distribution Function (BRDF) for lighting. McNally et al. [11] use a Phong BRDF without shadowing, citing computational intensity. Blacketer [12] implemented a Cook-Torrance BRDF for lighting with a plane stacking method for self-shadowing.

Methods for shape inversion fall into three major categories: Extended Gaussian Image (EGI), statistical estimation, and deep learning based methods, each approaching the problem from a different perspective.

Direct light curve inversion with the EGI uses a series of optimization problems to fit a convex shape to measurements. These methods were pioneered by Kaasalainen and Torppa for asteroids in [1] with simultaneous attitude inversion in [1]. While natural space objects like asteroids are largely convex, nearly all human-made space objects are highly non-convex, highlighting the need for a robust inversion scheme for both convex and non-convex space objects. The work of Kaasalainen et al. on asteroids was extended by Chng et al. [13] to find globally optimal spin pole and area vector solutions. Calef et al. [14] were early adopters of Kaasalainen and Torppa’s EGI methods for human-made objects, focusing on multispectrum measurements. Bradley and Axelrad [10] applied EGI methods to recover convex approximations of representative GEO objects. Fan and Frueh [3], [15], [16] used the EGI with a multi-hypothesis scheme to recover human-made object shapes with measurement noise. Friedman [4], [17] quantified the observability of EGI inversion to inform sensor tasking

schemes. Cabrera et al. [9] studied the effects of area regularization on Fan and Friedman’s methods to achieve more accurate reconstructions.

A second approach leverages statistical estimation to retrieve shape information. Linares et al. [18] applied an unscented Kalman filter to estimate attitude and convex shape simultaneously, representing shape with vertex displacement on a sphere. Linares et al. [19] used a Multiple-Model Adaptive Estimation (MMAE) algorithm to predict the truth geometry and attitude by comparing observations with a bank of reference objects. Linares and Crasidis **linares2017** used an Adaptive Hamiltonian Markov Chain Monte Carlo scheme to estimate shape and other characteristics simultaneously.

A third approach relies on deep learning. Linares and Furfaro [20] used a deep convolutional neural network to classify novel light curves as rocket bodies, payloads, or debris. Furfaro et al. [8] used similar methods classify novel light curves into four truth object classes. Kerr et al. [21] adapted the architecture developed by Furfaro et al. to classify object shape and size in an extended training set. McNally et al. [11] use AI and differential approaches to identify satellites from simulated and real light curves. Allworth et al. [7] applied transfer learning to simulated and real measurements to classify object type.

Various other unique methods have been applied to the light curve shape inversion problem. Hall et al. [22] investigated methods for independently solving shape parameters in isolation without attitude information. Fulcoy et al. [23] used measurements from different sensor locations to determine shape under various attitude profiles. Yanagisawa and Kurosaki [24] fit an analytical light curve model for a tri-axial ellipsoid to derive the shape and attitude profile of a Cosmos rocket body. Kobayashi applied compressed sensing to recover shape information from light curves by taking advantage of shadowing geometry [5], [25].

Shape inversion for non-convex objects — mainly asteroids — has been studied by others in the past. Durech and Kaasalainen [26] determined a relationship between concavity size and the minimum solar phase angle where self-shadowing impacts the light curve. Viikinkoski et al. [27] investigated recovering large concavities from adaptive optics imagery, noting the fundamental non-uniqueness of any solution. They discuss how a single large concavity may produce identical scattering behavior to multiple smaller concave features [27]. Cabrera et al.

[9] studied convex solutions for non-convex objects, concluding that the convex fit diverges from the true shape as the relative concavity size increases.

We approach the shape inversion problem with the foundational EGI optimization and object reconstruction methods of [1], [3]. The EGI optimization processes of [1], [3], [9] are improved using novel resampling and merging steps. These improvements circumvent the need for the regularization terms explored by Cabrera et al. [9]. We also address the reconstruction scaling issues present in Fan’s work [3] with an objective function proposed by Ikeuchi et al. [28] in place of Little’s [29]. The support optimization procedure is accelerated and strengthened with a preconditioning term proposed by Nicolet et al. [30], enabling the rapid reconstruction of more detailed convex objects than previously feasible.

Our approach has a number of general advantages. We do not require any *a priori* information about the truth geometry. Thus, unlike MMAE methods [19], we do not require a bank of reference models to recover shape information. Unlike deep learning methods, our method does not rely on the diversity of a training set to achieve realistic results [8], [21]. Our light curve simulation method improves on the facetwise ray traced shadows of [1], [3], [31] with shadow mapping, increasing shadow fidelity per unit computation time.

2.1 Coordinate Systems

2.1.1 International Terrestrial Reference Frame

The most intuitive Earth-centered reference frame is Earth-centered Earth-fixed (ECEF). An ECEF frame has its origin at the center of mass of the Earth and its axes fixed in the crust. The fundamental plane of the frame is defined to be the equator — defining the z -axis through Earth’s instantaneous spin axis, and the reference direction through the intersection of the prime meridian and the equator — defining the x -axis. Completing the right-handed system the y -axis yields a reference frame that remains fixed, neglecting continental drift and other pesky (but sufficiently negligible) realities.

2.1.2 Right Ascension and Declination

Right ascension and declination, often shortened to RA/Dec, are useful angles from describing the angular position of an object on the celestial sphere from the perspective of an observer. Right ascension is defined as the angle of the observation projected onto the inertial $x-y$ plane, measured counterclockwise from inertial \hat{x} , represented by α . Declination is the angle from the $x-y$ plane to the observation with positive values above the $x-y$ plane (closer to inertial z) and negative values below. Declination is represented by δ . Given a unit vector direction $\hat{v} = [x, y, z]^T$ in inertial space, we can compute RA/Dec via Eq 2.1.

$$\begin{bmatrix} \alpha \\ \delta \end{bmatrix} = \begin{bmatrix} \text{atan2}(y, x) \\ \text{atan2}(z, \sqrt{x^2 + y^2}) \end{bmatrix} \quad (2.1)$$

2.1.3 Azimuth and Elevation

Azimuth and elevation, often shortened to Az/El, are similar angular quantities to right ascension and declination, but instead of being based on the inertial sphere, they are referenced to an arbitrary reference frame. For a telescope making observations of an object, the local East-North-Up (ENU) frame may be used. For a satellite star tracker, star azimuth

and elevation might be reported in the satellite body frame. In either case, Eq 2.1 can be repurposed in terms of Az/El, where $\hat{v} = [x, y, z]^T$ is expressed in the frame of interest.

$$\begin{bmatrix} Az \\ El \end{bmatrix} = \begin{bmatrix} \text{atan2}(y, x) \\ \text{atan2}(z, \sqrt{x^2 + y^2}) \end{bmatrix} \quad (2.2)$$

Note that Eq 2.2 references azimuth to the x -axis, proceeding in the counterclockwise direction. Often, this reference axis and direction may be changed depending on the reference frame being used. For example, ground station observations may be referenced to local North — the second axis of the ENU system — proceeding clockwise. This would require the substitution $Az' = \frac{\pi}{2} - Az$. Notice that this substitution leads to Az' leaking outside the domain of $[0, 2\pi)$. This is not an issue for later coordinate transformations, but may be undesirable for plots. Wrapping the result back to the standard azimuth range via $Az_{wrapped} = \text{mod}(Az, 2\pi)$ is a sufficient fix.

3. MESHES

A computer represents 3D objects

4. ATTITUDE REPRESENTATIONS

When we talk about the orientation — also known as attitude — of a rigid body in three dimensions, that orientation is always implicitly understood to be relative to some other reference frame. The orientation of a book might be expressed using a frame fixed in the table it sits on. If that same book was sitting in an empty void, we would have no way to talk — or even think — about its orientation. Orientation itself is a three-dimensional quantity. Consider a coordinate system fixed in a rigid object and a second reference frame in which we want to express the orientation of the object. For convenience, we will call the frame fixed in the object the body frame, and the second frame the world frame. Any effective attitude representation must let us express the directions of all three body axes in terms of the world frame basis vectors. This raises an important question: how many numbers do we need to express an object’s attitude? We can express the direction of any unit vector with two numbers — the azimuth and elevation of that vector. Naïvely, we might extrapolate from this to conclude that we will need six numbers to express an orientation. Because the basis vectors form an orthonormal set $\{\hat{b}_1, \hat{b}_2, \hat{b}_3\}$, we know we can express $\hat{b}_3 = \hat{b}_1 \times \hat{b}_2$, $\hat{b}_2 = \hat{b}_3 \times \hat{b}_1$, and $\hat{b}_1 = \hat{b}_2 \times \hat{b}_3$. Each of these equations constrains one further degree of freedom, indicating that only three quantities are necessary to express the relative orientation of two reference frames. The most obvious parameterization for attitude is the direction cosine matrix (DCM), a 3×3 symmetric matrix with determinant 1. We notate the DCM with two capital letters, the rightmost indicating the reference frame of the input vectors and the leftmost indicating the transformed frame. Alternatively, the DCM is sometimes expressed as C when the frames involved are arbitrary or do not need to be denoted. For example, the DCM $[\mathcal{B}\mathcal{N}]$ takes vectors in the \mathcal{N} frame to the \mathcal{B} frame:

$${}^{\mathcal{B}}\mathbf{r} = [\mathcal{B}\mathcal{N}]^{\mathcal{N}}\mathbf{r} \quad (4.1)$$

The orthogonal property of the DCM implies $[\mathcal{B}\mathcal{N}]^{-1} = [\mathcal{B}\mathcal{N}]^T$ such that $[\mathcal{B}\mathcal{N}]^T = [\mathcal{N}\mathcal{B}]$.

Another core attitude representation is the Euler angle-axis form. Euler’s rotation theorem guarantees that any relative orientation can be expressed as a single rotation about an axis $\hat{\lambda} \in \mathbb{S}^2$ by an angle $\theta \in [0, 2\pi]$. The set $\{\hat{\lambda}, \theta\}$ is known as a principal rotation

parameter, abbreviated PRP hereafter. The DCM is mapped to the PRP representation via [32]

$$\theta = \cos^{-1} \left(\frac{1}{2} [C_{1,1} + C_{2,2} + C_{3,3} - 1] \right) \quad (4.2)$$

$$\hat{\lambda} = \frac{1}{2 \sin \theta} \begin{bmatrix} C_{2,3} - C_{3,2} \\ C_{3,1} - C_{1,3} \\ C_{1,2} - C_{2,1} \end{bmatrix} \quad (4.3)$$

Where $C_{i,j}$ refers to the i th row and j th column of C . The mapping from PRP to DCM is also relatively straightforward:

$$C = I_3 + \sin \theta [\hat{\lambda} \times] + (1 - \cos \theta) [\hat{\lambda} \times]^2 \quad (4.4)$$

Where $[v \times]$ is the matrix cross product operator, defined on $\mathbf{v} \in \mathbb{R}^3$ as:

$$[\mathbf{v} \times] = \begin{bmatrix} 0 & -v_3 & v_2 \\ v_3 & 0 & -v_1 \\ -v_2 & v_1 & 0 \end{bmatrix} \quad (4.5)$$

This operator is useful in that it takes care of cross products for us, i.e. $\mathbf{v} \times \mathbf{u} = [\mathbf{v} \times] \mathbf{u}$. While the PRP $\{\theta, \hat{\lambda}\}$ is a four element set, there are only three degrees of freedom due to the unit norm constraint on $\hat{\lambda}$. This means that we can multiply the Euler angle by the axis, yielding a closely related attitude representation known as the rotation vector (RV), generally denoted \mathbf{p} .

$$\mathbf{p} = \theta \hat{\lambda} \quad (4.6)$$

The RV is the first truly three dimensional representation we have come across so far. This is advantageous for visualizing sets of orientations, but there are multiple notable issues with any three dimensional embedding of $SO(3)$. Any representation embedded in \mathbb{R}^3 loses

	DCM	PRP	RV	MRP
DCM	—			
PRP	$C = I_3 + \sin \theta \left[\hat{\lambda} \times \right] + (1 - \cos \theta) \left[\hat{\lambda} \times \right]^2$	—	$\mathbf{p} = \theta \hat{\lambda}$	
RV			—	
MRP				—

some of the spherical qualities of \mathbb{S}^3 , leading to singularities — regions where attitudes are not uniquely defined or are impossible to compute in the first place.

To summarize, we can transform to and from all attitude representations with relatively simple algebraic operations:

5. LIGHTING

Although light curves come from unresolved measurements, the interactions that produce them are directly driven by the shape and material properties of the object being observed. In order to simulate accurate light curves, we must model all important optical interactions. In broad terms, this boils down to determining how the object is lit and how it is shadowed.

At the microscopic scale, the surface of an object is composed of facets — small areas sharing a normal vector. The macroscopic optical properties of the material is driven by the distribution of sizes and normal directions of the facets. If the facets are distributed in biased orientations, the macroscopic surface may show anisotropy, leading to the appearance of brushed metal. If the facets normals are at large angles to each other, the surface may appear dull as the outgoing direction of the light may be completely independent from the incoming direction. Subsurface effects — where incoming light rays scatter *inside* the surface can also change the macroscopic properties of the material.

This discussion raises an important question; how can we model the macroscopic outcomes of the true microscopic interactions of incident light on a surface? The bidirectional reflectance distribution function (BRDF) is a tool developed in computer graphics to address this exact problem. The BRDF is a function on the hemisphere which expresses the fraction of light per solid angle (radiance \mathcal{R}) leaving the surface in a given direction, divided by the incident power per unit area (irradiance \mathcal{I}). The general formulation for a BRDF f_r is given by: [33]

$$f_r(\mathbf{x}, L \rightarrow O) = \frac{d\mathcal{R}(\mathbf{x} \rightarrow O)}{d\mathcal{I}(L \rightarrow \mathbf{x})}. \quad (5.1)$$

In Equation 5.1, $\mathbf{x} \in \mathbb{R}^3$ is the point on the object’s surface the BRDF is evaluated at. $L \in \mathbb{S}^2$ is the incoming illumination unit vector and $O \in \mathbb{S}^2$ is the outgoing unit vector. This definition is useful for building intuition about the form of the BRDF, but to represent a physically plausible reflection process, a candidate function must satisfy a few additional constraints. Assuming that the material is not luminescent, more light cannot be reflected from a unit of surface area than what hit it. This means that integrating the BRDF over

the hemisphere centered around the surface normal vector should yield a value smaller or equal to one.



Figure 5.1. By default figures are not centered. This is a long caption to demonstrate that captions are single spaced. This is a long caption to demonstrate that captions are single spaced.

6. Light Curves

A light curve is a time series of unresolved optical brightness measurements. Once an object is far enough away from the observer to become unresolved, all geometric data is lost and the only information that remains in the individual measurements is the total brightness. "Brightness" is a catch-all term for a variety of units.

6.1 Brightness Units

6.1.1 Irradiance

Irradiance is the standard SI linear unit used to describe the total amount of energy incident on a surface from a given source. An irradiance of $1 \left[\frac{W}{m^2} \right]$ implies that a $10 [m]$ area would experience $10 [W]$ of incident energy. The Sun's irradiance is approximately $1361 \left[\frac{W}{m^2} \right]$ at a distance of 1 AU.

Visual magnitude — also known as apparent or relative magnitude — is a reverse logarithmic scale that originates in astronomy. Stellar sources span many orders of magnitude of brightness, making a logarithmic scale a helpful middle ground for comparison. Note that apparent magnitude always expresses brightness at the observer's location; absolute magnitude is a different quantity that normalizes brightness from a distance of 10 parsecs. In terms of irradiance, apparent magnitude is computed via Eq 6.1.

$$m = -2.5 \log_{10} \left(\frac{I}{I_0} \right) \quad (6.1)$$

In Eq 6.1, I is the irradiance of the source of interest and I_0 is irradiance of the zero-point source. This makes sense as if we plug in $I = I_0$, we are left with $m = 0$. The star Vega is usually taken to be the zero-point with irradiance $I_0 = 2.518021002 \cdot 10^{-8} \left[\frac{W}{m^2} \right]$.

We can rearrange Eq 6.1 to compute irradiance from a given apparent magnitude, yielding Eq 6.2

$$I = I_0 \cdot 10^{-\frac{m}{2.5}} \quad (6.2)$$

6.1.2 Normalized Irradiance

This work also uses normalized irradiance, the irradiance of a source if the observer was 1 meter away. This is a non-standard quantity in the literature, but proves useful for the same reasons absolute magnitude is used by astronomers. Adjusting sources to be at a standard distance allows us to simulate and invert light curves in a non-dimensionalized space, simplifying simulation and making the inversion optimizations more robust. To make the conversion explicit, irradiance observed at a distance r in meters from an object is converted to normalized irradiance \hat{I} in Watts via Eq 6.3

$$\hat{I} = r^2 I \quad (6.3)$$

6.1.3 Candela

Some light pollution datasets are given in units that include candela. Candela is the SI base unit of luminous intensity defined by the International Committee for Weights and Measures as "Fixing the numerical value of the luminous efficacy of monochromatic radiation of frequency $540 \cdot 10^{12}$ Hz to be equal to exactly 683" [34]. This means that an isotropic source with frequency $540 \cdot 10^{12}$ Hz ($\lambda = 555$ nm) has a luminous efficacy of $K_{cd} = 683$ [lm/W] where lm stands for lumens. Luminous efficacy itself determines how well a source produces visible light.

6.1.4 S_{10}

While magnitude and irradiance do a good job describing the flux of point sources, other units exist to talk about diffuse or extended sources where brightness is somewhat uniformly spread over an area. S_{10} is a unit of surface brightness represented by the number of 10th magnitude stars per square degree that would produce the same flux. Surface brightness in S_{10} over a given solid angle Ω [rad²] can be converted to total irradiance I [$\frac{W}{m^2}$] via Eq 6.4.

$$\frac{I \left[\frac{W}{m^2} \right]}{S_{10}} = 10^{-10/2.5} \left(\Omega \frac{180^2}{\pi^2} \right) \int_{10^{-8}}^{10^{-6}} \text{STRINT}(\lambda) d\lambda = 8.26617 \Omega \cdot 10^{-9} \quad (6.4)$$

In 6.4, $\text{STRINT}(\lambda) \left[\frac{W}{m^2 \cdot m} \right]$ is the representative spectrum of a 0th magnitude star, $\text{QE}(\lambda)$ is the quantum efficiency spectrum of the observing sensor, $\text{ATM}(\lambda)$ is the atmospheric transmission spectrum, $\lambda [m]$ is wavelength, $h \left[\frac{m^2 \cdot kg}{s} \right]$ is Plank's constant, and $c \left[\frac{m}{s} \right]$ is the speed of light in vacuum.

6.1.5 Magnitudes per Square Arcsecond

A second surface brightness unit is $\left[\frac{mag}{arcsec^2} \right]$. This quantity can be thought of as a generalized S_{10} , where instead of quantifying the number of stars of a certain magnitude in a solid angle, we measure the equivalent magnitude of a single point source. A surface brightness B_{10} in S_{10} can be converted into surface brightness B_{mag} in $\left[\frac{mag}{arcsec^2} \right]$ via Eq 6.5.

$$B_{mag} = -2.5 \log_{10} \left(\frac{B_{10} \cdot 10^{-4}}{12960000} \right) \quad (6.5)$$

In Eq 6.5 we first convert S_{10} to the total irradiance per square degree, convert square degrees to square arcseconds, and transform the result back into apparent magnitude.

6.1.6 Photoelectron Counts

Raw observations of brightness taken by a CCD-equipped telescope are measured in photoelectron counts, otherwise known as Analog-to-Digital Units (ADU) [35]. The count in a single pixel obtained is directly proportional (via the ADU gain) to the number of photons incident on that pixel during the integration time. Higher order effects in the silicon of the CCD makes this statement incomplete at best, but for the non-resolved imaging applications we're concerned about, chip-level inaccuracies besides readout noise and dark current are often neglected [36]. Irradiance can be converted back and forth to ADU via the conversion factor $SINT$ in Eq 6.6 [35].

$$SINT = \frac{\pi D^2}{4} \int_{10^{-8}}^{10^{-6}} \left(\frac{SUN(\lambda)}{I_{sun}} \right) \cdot \text{QE}(\lambda) \cdot \text{ATM}(\lambda) \cdot \left(\frac{\lambda}{hc} \right) d\lambda \quad (6.6)$$

In Eq 6.6, $SUN(\lambda)$ is the spectrum of solar irradiance in $\left[\frac{W}{m^2 \cdot m} \right]$, I_{sun} is the irradiance of the Sun (generally taken to be the solar constant $1361 \left[\frac{W}{m^2} \right]$). Read literally, the integral term

as units $\left[\frac{1}{W_s}\right]$, giving the number of counts per incident Watt of solar radiation and second of integration time. The aperture diameter factor outside the integral accounts for the area of light incident on the CCD, giving SINT units of $\left[\frac{m^2}{W_s}\right]$. Multiplying by irradiance in $\left[\frac{W}{m^2}\right]$ and an integration time Δt in seconds will yield the count of photoelectrons S in ADU as shown in Eq 6.7.

$$S = \text{SINT} \cdot I \cdot \Delta t \quad (6.7)$$

For completeness, irradiance can be recovered from a signal in ADU and the integration time via Eq 6.8.

$$I = \frac{S}{\text{SINT} \cdot \Delta t} \quad (6.8)$$

6.2 Astronomical Spectra

Four of the quantities needed for the background model vary with wavelength. These are the atmospheric transmission, the sensor quantum efficiency, the irradiance of a 0th magnitude star, and the solar spectrum. Atmospheric transmission is a unitless quantity conveying the fraction of light that is not absorbed by the atmosphere. Quantum efficiency is a unitless quantity which conveys the fraction of incident photons which are (proportionally) converted to photoelectrons in the CCD sensor. Each spectrum is displayed in Figure 6.1.

In practice, the quantum efficiency curve varies by sensor and the thermal conditions of the observation. The curve adopted in this work is that used by Krag; modern sensors will often perform better.

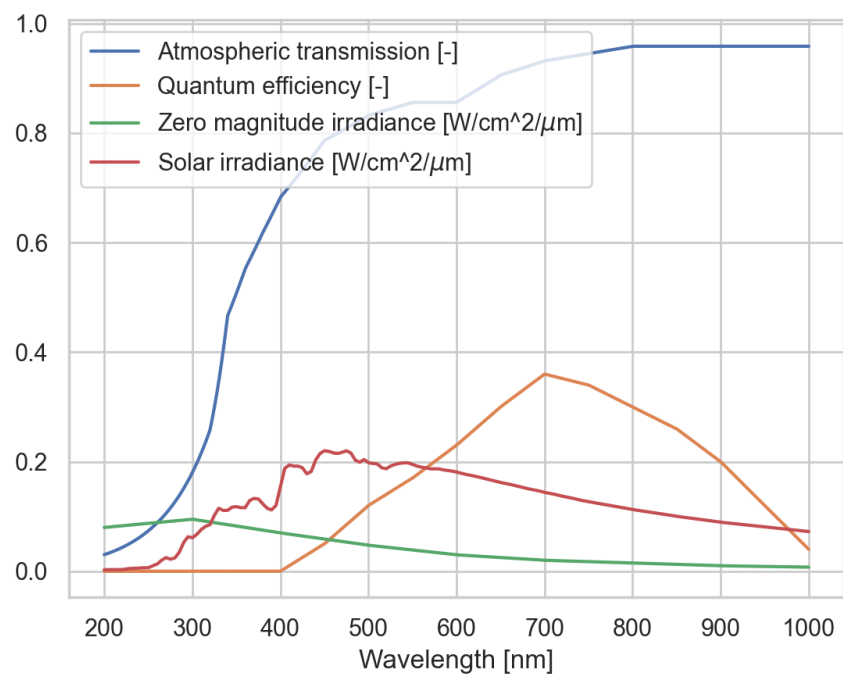


Figure 6.1. Astronomical Spectra

7. Background Signals

Whenever an optical telescope is observing a space object, the object’s signal is necessarily superimposed on whatever signals exist in the background. In this context, background does not only refer to sources physically further than the object, but all sources that impact the image apart from the object signal. As we will see, some of these sources even originate within the telescope. To faithfully simulate a telescope observing an object, many position-based SDA tasks are able to ignore background effects while acquiring or tracking objects. For photometry-based SDA, the background is critical. Background signals can be broken up into atmospheric effects, exoatmospheric effects, and sensor effects.

7.1 Atmospheric Effects

7.1.1 Airglow

Certain chemical reactions from 80-110 km altitude in the upper atmosphere release visible light [35]. This effect is known as airglow. Since these reactions are assumed to be isotropic — equally intense when integrated along any vertical line extending upwards from the surface. We model the airglow signal AINT in a similar fashion to integrated starlight. Given the airglow spectra $\text{GLINT}(\lambda)$ $\left[\frac{W}{m^2 \cdot m \cdot rad^2}\right]$, we compute Eq 7.1.

$$\text{AINT} = \frac{\pi D^2}{4} \int_{10^{-8}}^{10^{-6}} \text{GLINT}(\lambda) \cdot \text{QE}(\lambda) \cdot \text{ATM}(\lambda) \cdot \left(\frac{\lambda}{hc}\right) d\lambda \quad (7.1)$$

The quantity AINT has units $\left[\frac{1}{s \cdot rad^2}\right]$, meaning that the airglow signal in ADU is simply given by Eq 7.2

$$van_{rhijn} \quad (7.2)$$

In Eq 7.2, $\frac{1}{\cos(\theta_z)}$ is known as the Van Rhijn factor, which accounts for the accumulation of airmass near the horizon ??.

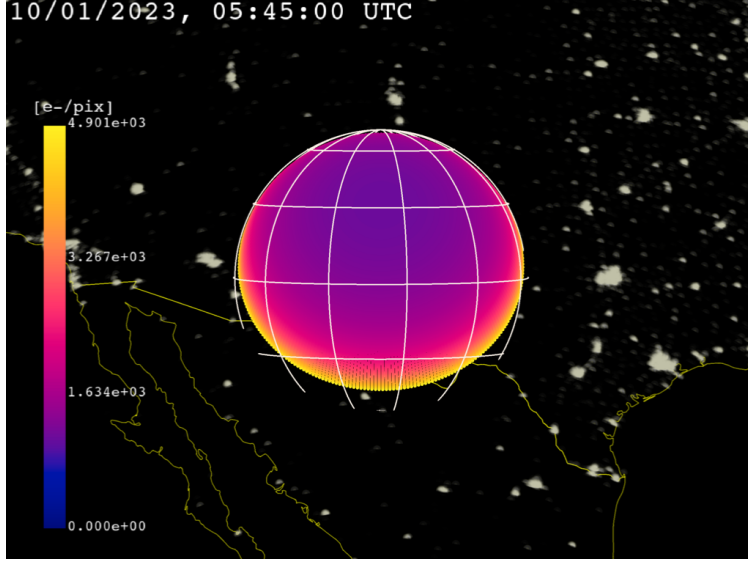


Figure 7.1. Airglow signal on the local observer hemisphere. The observer is in New Mexico, USA at 32.900° N, -105.533° W

7.1.2 Light Pollution

The final source of background noise light pollution. On a cloudless night with negligible light pollution, the zenith surface brightness is approximately $22 \left[\frac{\text{mag}}{\text{arcsec}^2} \right]$ [35]. As light pollution increases, this zenith brightness may dip down to $14 - 15 \left[\frac{\text{mag}}{\text{arcsec}^2} \right]$. To get accurate localized zenith brightness values, we use the 2015 World Atlas of Sky Brightness [37]. The data is reported in $\left[\frac{\text{mcd}}{\text{m}^2} \right]$

7.2 Exoatmospheric Effects

7.2.1 Integrated Starlight

Stars are almost always present in optical images of space objects. The brightest stars streaking across the field of view in REFFIGBELOW have high SNRs and stand out clearly against the dark background. This raises a question: if we're observing a full $1^\circ \times 1^\circ$ area of the sky, where are the rest of the stars given that the Milky Way alone contains approximately $1 \cdot 10^{11}$ stars? The answer is relatively obvious: many more stars are present in the image

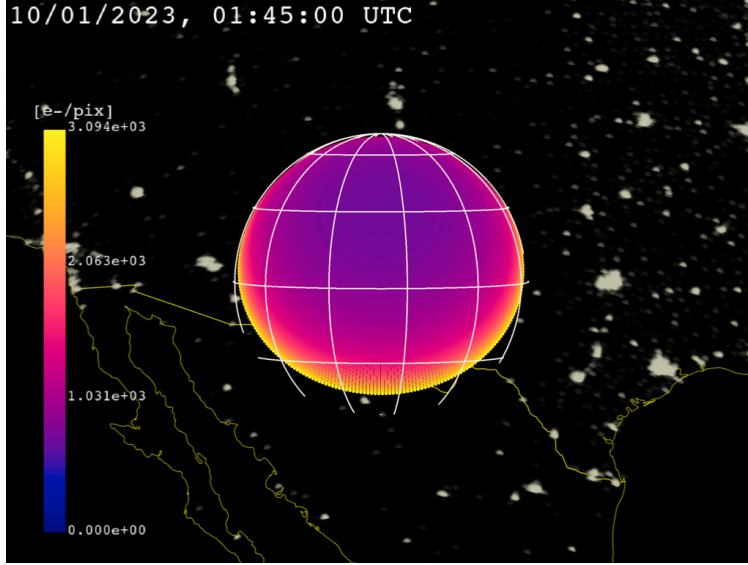


Figure 7.2. Light pollution signal on the local observer hemisphere. The observer is in New Mexico, USA at 32.900° N, -105.533° W

than we can pick out individually, most of them fall into the background. We call this residual faint starlight "integrated" starlight as we are effectively integrating the signals from thousands or millions of stars across the image plane.

Most stars are too faint to appear as points of light on the image plane. Instead, they merge into the background. The signal due to these faint stars is known as integrated starlight. Krag [35] modeled this signal by building a $1^\circ \times 1^\circ$ grid of surface brightness values for the full right ascension (RA) and declination (Dec) sphere. Krag used the Guide Star catalog, which contains 15 million stars down to magnitude 16. Exponential extrapolation was used to predict star counts in each bin for higher magnitudes [35]. Twenty years later, we have access to larger star catalogs that are nearly complete to much dimmer magnitudes. The integrated starlight catalog used in this work was built from the GAIA catalog with approximately 1.5 billion stars down to magnitude 21-22 [38]. The same $1^\circ \times 1^\circ$ grid was computed using the `astroquery.gaia` Python package [39]. Figure 7.4 shows the computed patched catalog, in units of S_{10} .



Figure 7.3. Raw image of three GEO objects with stars streaking through the background. Taken by the Purdue Optical Ground station at 32.900° N, -105.533° W by Nathan Houtz

Now that we have a data source for the exoatmospheric mean brightness of the night sky due to integrated starlight, we can compute the corresponding signal mean for a telescope equipped with a CCD sensor. Again, we adopt Krag’s formulation [35].

$$\text{BINT} = \frac{\pi D^2}{4} \int_{10^{-8}}^{10^{-6}} \text{STRINT}(\lambda) \cdot \text{QE}(\lambda) \cdot \text{ATM}(\lambda) \cdot \left(\frac{\lambda}{hc} \right) d\lambda \quad (7.3)$$

In Eq 7.3, D is the telescope aperture diameter in meters, h is Plank’s constant in $\left[\frac{m^2 kg}{s} \right]$, and c is the speed of light in vacuum in $\left[\frac{m}{s} \right]$. The resulting quantity BINT has units of $\left[\frac{1}{s} \right]$, representing the mean total photons passing through the telescope aperture due to integrated starlight.

$$\bar{S}_{star} = 10^{-4} \cdot \text{BINT} \cdot \left(\frac{s}{3600} \right)^2 \cdot \Delta t \cdot b_{cat} \quad (7.4)$$

In Eq 7.4, b_{cat} is the patched catalog brightness in $[S_{10}]$, s is the telescope pixel scale in $\left[\frac{\text{arcsecond}}{\text{pix}} \right]$, and Δt is the integration time in seconds. Note the addition of the 10^{-4}

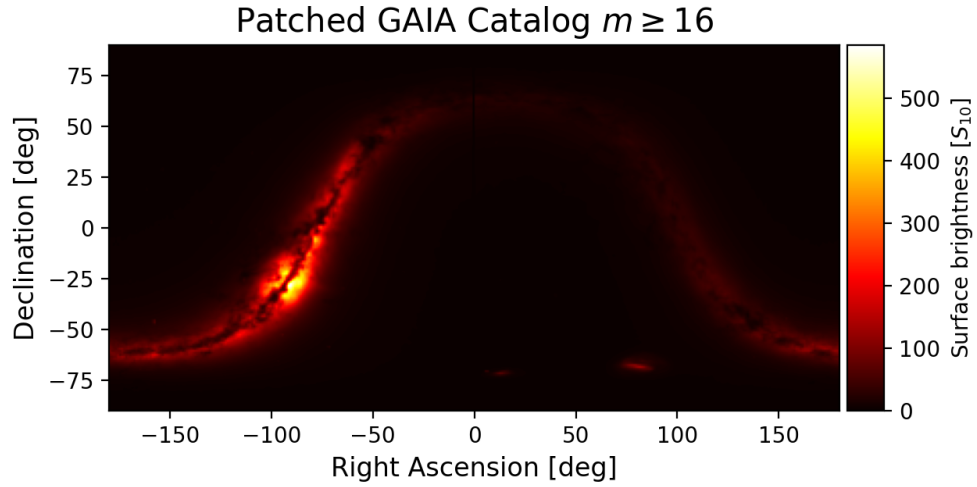


Figure 7.4. Integrated starlight patched catalog

factor to reconcile catalog surface brightness in terms of 10th magnitude stars, and the 0th magnitude source in BINT. This yields \bar{S}_{star} with units $\left[\frac{e^-}{pix^2}\right]$; photoelectron counts per pixel area. Figure 7.5 shows the background signal mean due to integrated starlight.

7.2.2 Scattered Moonlight

7.2.3 Zodiacal Light

7.3 Sensor Effects

7.3.1 Dark Noise

7.3.2 Readout Noise

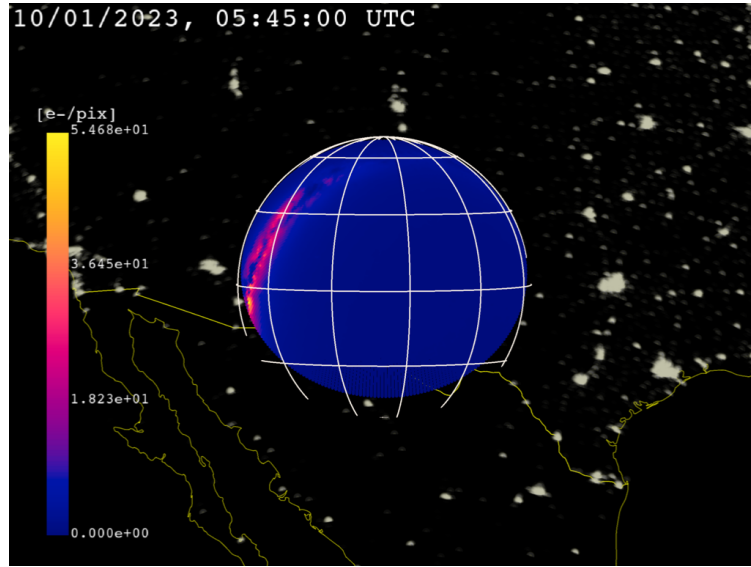


Figure 7.5. Integrated starlight signal on the local observer hemisphere. The observer is in New Mexico, USA at 32.900° N, -105.533° W

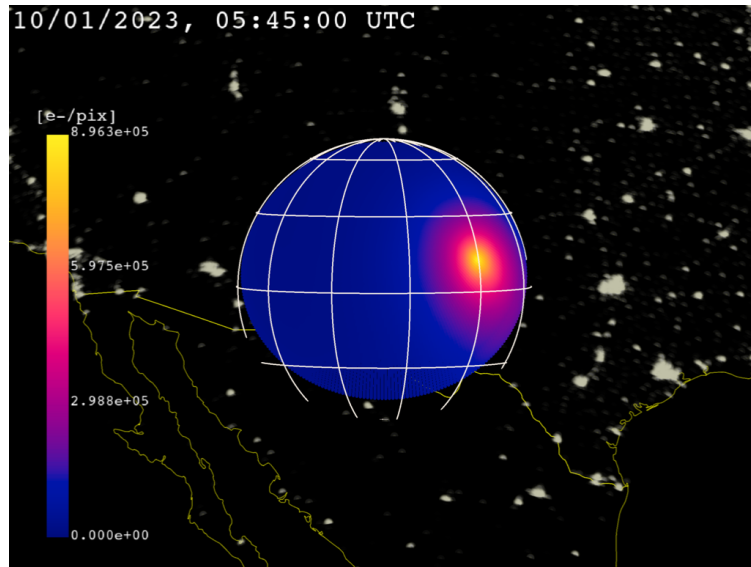


Figure 7.6. Scattered moonlight signal on the local observer hemisphere. The observer is in New Mexico, USA at 32.900° N, -105.533° W

8. Light Curve Simulation

8.0.1 Simulating Convex Objects

Light curve simulation for convex geometry can be solved semi-analytically as each facet's contribution to the measured irradiance can be computed individually [1]. Determining whether a face is illuminated requires two horizon checks to determine visibility from the Sun and to the observer. For a facet i at timestep j these horizon checks are expressed by the shadowing condition μ_{ij} .

$$\mu_{ij} = \begin{cases} 1 & \text{if } (\hat{O}_j \cdot \hat{n}_i) > 0 \text{ and } (\hat{S}_j \cdot \hat{n}_i) > 0 \text{ and } \delta_{ij,ss} = 0 \text{ and } \delta_{ij,os} = 0 \\ 0 & \text{otherwise} \end{cases} \quad (8.1)$$

The unit vectors \hat{O} and \hat{S} point from the center of mass of the object to the observer and Sun, respectively. We choose the outward-pointing facet normal unit vector \hat{n} by convention for all mesh operations. The self-shadowing and observer-shadowing conditions, $\delta_{ij,ss}$ and $\delta_{ij,os}$, are always zero for convex polyhedra but are crucial for accurately simulating non-convex geometry. For objects with concavities, self-shadowing refers to shadows cast by an object onto itself and observer-shadowing refers to otherwise visible faces blocked by other portions of the geometry.

The irradiance I received by the observer at timestep j is the sum of the received irradiance from all facets, composed of specular and diffuse contributions. We express each contribution as the product of the normalized irradiance \hat{I} . This can be scaled to adjust for the distance from the observer to the object to yield the noiseless received irradiance.

9. Appendices

9.1 Astronomical Spectra Data

Atmospheric Extinction

```
{"lambda": [0.0, 3.2e-07, 3.4000000000000003e-07, 3.6e-07, 3.7999999999999996e-07,
4e-07, 4.5e-07, 5e-07, 5.5e-07, 6e-07, 6.5e-07, 7e-07, 8e-07, 0.001], "extinction":
[5.0, 0.96, 0.54, 0.42, 0.34, 0.27, 0.17, 0.13, 0.11, 0.11, 0.07, 0.05, 0.03, 0.0]}
```

Quantum Efficiency

```
{"lambda": [4.0000000000000003e-07, 4.5000000000000003e-07, 5.000000000000001e-07,
5.5e-07, 6.000000000000001e-07, 6.5e-07, 7.000000000000001e-07, 7.5e-07,
8.000000000000001e-07, 8.5e-07, 9.000000000000001e-07, 9.5e-07,
1.0000000000000002e-06, 1.0500000000000001e-06], "quantum_efficiency": [0.0, 0.05,
0.12, 0.17, 0.23, 0.3, 0.36, 0.34, 0.3, 0.26, 0.2, 0.12, 0.04, 0.0]}
```

9.1.1 Background Source Data

Lunar Phase Factor

```
{"phase_factor": [1.00, 0.809, 0.685, 0.483, 0.377, 0.288, 0.225, 0.172, 0.127, 0.089,
0.061, 0.041, 0.077, 0.017, 0.009, 0.004, 0.001, 0.0, 0.0], "phase_angle": [0,
0.17453293, 0.34906585, 0.52359878, 0.6981317 , 0.87266463, 1.04719755, 1.22173048,
1.3962634 , 1.57079633, 1.74532925, 1.91986218, 2.0943951 , 2.26892803, 2.44346095,
2.61799388, 2.7925268 , 2.96705973, 3.14159265]}
```

Scattered Moonlight

```
{"z_obs": [0.0, 0.17453292519943295, 0.3490658503988659, 0.5235987755982988,
0.6981317007977318, 0.8726646259971648, 1.0471975511965976, 1.2217304763960306,
1.3962634015954636], "delta_az": [0.0, 0.7853981633974483, 1.5707963267948966,
2.356194490192345, 3.141592653589793], "z_moon": [0.0, 0.5235987755982988,
1.0471975511965976, 1.3089969389957472], "radiance": [[[22.0, 19.0, 13.0, 10.0],
[22.0, 19.0, 13.0, 10.0], [22.0, 19.0, 13.0, 10.0], [22.0, 19.0, 13.0, 10.0], [22.0,
19.0, 13.0, 10.0]], [[22.0, 21.0, 15.0, 11.0], [22.0, 20.0, 14.0, 11.0], [22.0,
19.0, 13.0, 10.0], [22.0, 18.0, 12.0, 9.7], [22.0, 18.0, 12.0, 9.6]], [[22.0, 23.0,
18.0, 13.0], [22.0, 22.0, 16.0, 12.0], [22.0, 19.0, 14.0, 10.0], [22.0, 17.0, 12.0,
9.9], [22.0, 17.0, 12.0, 10.0]], [[22.0, 25.0, 21.0, 16.0], [22.0, 23.0, 18.0,
14.0], [22.0, 20.0, 14.0, 11.0], [22.0, 17.0, 12.0, 11.0], [22.0, 16.0, 12.0,
11.0]], [[23.0, 28.0, 25.0, 20.0], [23.0, 25.0, 21.0, 17.0], [23.0, 21.0, 16.0,
12.0], [23.0, 17.0, 14.0, 13.0], [23.0, 16.0, 14.0, 14.0]], [[24.0, 31.0, 31.0,
25.0], [24.0, 28.0, 26.0, 20.0], [24.0, 22.0, 18.0, 15.0], [24.0, 18.0, 17.0, 16.0],
[24.0, 18.0, 18.0, 18.0]], [[27.0, 37.0, 39.0, 33.0], [27.0, 33.0, 32.0, 26.0],
[27.0, 25.0, 22.0, 18.0], [27.0, 22.0, 22.0, 21.0], [27.0, 22.0, 25.0, 26.0]],
[[34.0, 47.0, 54.0, 48.0], [34.0, 41.0, 43.0, 37.0], [34.0, 33.0, 29.0, 25.0],
[34.0, 30.0, 33.0, 32.0], [34.0, 31.0, 40.0, 40.0]], [[55.0, 72.0, 89.0, 82.0],
[55.0, 65.0, 71.0, 63.0], [55.0, 54.0, 50.0, 43.0], [55.0, 54.0, 61.0, 58.0], [58.0,
58.0, 76.0, 75.0]]]]}
```

Zodiacal Light

```
{"ecliptic_lat": [0.0, 0.17453292519943295, 0.3490658503988659, 0.5235987755982988,
0.6981317007977318, 0.8726646259971648, 1.0471975511965976, 1.2217304763960306,
1.3962634015954636], "ecliptic_lon": [3.141592653589793, 2.792526803190927,
2.443460952792061, 2.0943951023931953, 1.7453292519943295, 1.3962634015954636,
1.1344640137963142, 1.0471975511965976, 0.9599310885968813, 0.8726646259971648,
0.7853981633974483, 0.6981317007977318, 0.6108652381980153, 0.5235987755982988,
0.4363323129985824, 0.3490658503988659, 0.2617993877991494, 0.17453292519943295,
0.08726646259971647, 0.0], "brightness": [[258.0, 211.0, 206.99999999999997, 239.0,
277.0, 365.0, 535.0, 630.0, 756.0, 939.0, 1190.0, 1490.0, 2010.0000000000002,
2940.0, 4660.0, 7690.000000000001, 15100.0, 36500.0, 176000.0, 163000000.0], [212.0,
194.0, 185.0, 217.0, 247.00000000000003, 312.0, 418.0, 455.0, 512.0, 603.0, 696.0,
825.0, 1150.0, 1550.0, 1820.0, 2140.0, 2760.0, 2720.0, 5630.0, 19900.0], [183.0,
174.0, 168.0, 196.0, 220.00000000000003, 258.0, 330.0, 339.0, 358.0, 403.0, 442.0,
512.0, 635.0, 800.0, 932.0, 1070.0, 1120.0, 1390.0, 1700.0, 2290.0], [159.0, 153.0,
152.0, 177.0, 196.0, 219.0, 258.0, 270.0, 282.0, 290.0, 304.0, 331.0, 363.0, 417.0,
491.0, 542.0, 592.0, 655.0, 724.0, 794.0], [141.0, 137.0, 137.0, 161.0, 175.0,
190.0, 204.0, 212.0, 229.0, 227.0, 233.0, 240.0, 224.00000000000003, 241.0, 246.0,
252.0, 265.0, 290.0, 315.0, 403.0], [127.0, 127.0, 128.0, 146.0, 156.0, 166.0,
165.0, 166.0, 183.0, 185.0, 189.0, 186.0, 171.0, 180.0, 183.0, 186.0, 190.0, 199.0,
209.0, 252.0], [117.0, 120.0, 120.0, 132.0, 139.0, 146.0, 137.0, 137.0, 147.0,
149.0, 150.0, 149.0, 137.0, 141.0, 144.0, 145.0, 145.0, 145.0, 146.0, 150.0],
[110.00000000000001, 112.00000000000001, 112.00000000000001, 120.0, 123.0, 127.0,
118.0, 120.0, 124.0, 124.0, 124.0, 126.0, 118.0, 120.0, 121.0, 121.0, 121.0, 121.0,
121.0, 121.0], [103.0, 105.0, 105.0, 108.0, 111.00000000000001, 111.00000000000001,
106.0, 107.0, 107.0, 108.0, 107.0, 111.00000000000001, 107.0, 106.0, 108.0, 108.0,
108.0, 108.0, 108.0, 108.0]]}
```

REFERENCES

- [1] M. Kaasalainen, J. Torppa, and K. Muinonen, “Optimization methods for asteroid lightcurve inversion: Ii. the complete inverse problem,” *Icarus*, vol. 153, no. 1, pp. 37–51, 2001, ISSN: 0019-1035. DOI: <https://doi.org/10.1006/icar.2001.6674>. [Online]. Available: <https://www.sciencedirect.com/science/article/pii/S0019103501966746>.
- [2] S. Fan, C. Frueh, and A. Buzzoni, “A light curve simulation of the apollo lunar ascent module,” in *AIAA/AAS Astrodynamics Specialist Conference*, 2016, pp. 1–10. DOI: [10.2514/6.2016-5504](https://doi.org/10.2514/6.2016-5504).
- [3] S. Fan, “The light curve simulation and its inversion problem for human-made space objects,” Ph.D. dissertation, Purdue University, Aug. 2020. DOI: [10.25394/PGS.12749570.v1](https://doi.org/10.25394/PGS.12749570.v1).
- [4] A. M. Friedman, “Observability analysis for space situational awareness,” Ph.D. dissertation, Purdue University, Apr. 2020. DOI: [10.25394/PGS.12196863.v1](https://doi.org/10.25394/PGS.12196863.v1).
- [5] D. Kobayashi and C. Frueh, “Compressed sensing for satellite characterization,” in *Proceedings of the 20th AAS/AIAA Astrodynamics Specialist Conference*, Aug. 2020, pp. 1–20.
- [6] J. Allworth, L. Windrim, J. Wardman, D. Kucharski, J. Bennett, and M. Bryson, “Development of a high fidelity simulator for generalised photometric based space object classification using machine learning,” in *Proceedings of 70th International Astronautical Congress*, International Astronautical Congress, 2019, pp. 1–14. DOI: [10.48550/ARXIV.2004.12270](https://doi.org/10.48550/ARXIV.2004.12270). [Online]. Available: <https://arxiv.org/abs/2004.12270>.
- [7] J. Allworth, L. Windrim, J. Bennett, and M. Bryson, “A transfer learning approach to space debris classification using observational light curve data,” *Acta Astronautica*, vol. 181, pp. 301–315, Jan. 2021. DOI: [10.1016/j.actaastro.2021.01.048](https://doi.org/10.1016/j.actaastro.2021.01.048).
- [8] R. Furfaro, R. Linares, and V. Reddy, “Shape Identification of Space Objects via Light Curve Inversion Using Deep Learning Models,” in *Proceedings of the 20th Advanced Maui Optical and Space Surveillance Technologies Conference*, S. Ryan, Ed., Sep. 2019, 17, p. 17.

- [9] D. V. Cabrera, J. Utzmann, and R. Förstner, “Inversion of the shape of space debris from non-resolved optical measurements within spook,” in *Proceedings of the 22nd Advanced Maui Optical and Space Surveillance Technologies Conference*, 2021, pp. 1–18.
- [10] B. K. Bradley and P. Axelrad, “Lightcurve inversion for shape estimation of geo objects from space-based sensors,” in *Proceedings of the International Symposium on Space Flight Dynamics*, 2014, pp. 1–20.
- [11] K. McNally, D. Ramirez, A. M. Anton, D. Smith, and J. Dick, “Artificial intelligence for space resident objects characterisation with lightcurves,” in *Proceedings of the 8th European Conference on Space Debris*, ESA Space Debris Office, 2021, pp. 1–12.
- [12] L. D. J. Blacketer, “Attitude characterisation of space objects using optical light curves,” Ph.D. dissertation, University of Southampton, Mar. 2022. [Online]. Available: <https://eprints.soton.ac.uk/457200/>.
- [13] C.-K. Chng, M. Sasdelli, and T.-J. Chin, “Globally optimal shape and spin pole determination with light-curve inversion,” *Monthly Notices of the Royal Astronomical Society*, vol. 513, no. 1, pp. 311–332, Jan. 2022, ISSN: 0035-8711. DOI: [10.1093/mnras/stac198](https://doi.org/10.1093/mnras/stac198). eprint: <https://academic.oup.com/mnras/article-pdf/513/1/311/43446894/stac198.pdf>. [Online]. Available: <https://doi.org/10.1093/mnras/stac198>.
- [14] B. Calef, J. Africano, B. Birge, D. Hall, and P. Kervin, “Photometric signature inversion,” in *Unconventional Imaging II*, V. L. Gamiz, P. S. Idell, and M. S. Strojnik, Eds., International Society for Optics and Photonics, vol. 6307, SPIE, 2006, pp. 141–150. DOI: [10.1117/12.683015](https://doi.org/10.1117/12.683015). [Online]. Available: <https://doi.org/10.1117/12.683015>.
- [15] S. Fan and C. Frueh, “A direct light curve inversion scheme in the presence of measurement noise,” *The Journal of the Astronautical Sciences*, vol. 67, Aug. 2019. DOI: [10.1007/s40295-019-00190-3](https://doi.org/10.1007/s40295-019-00190-3).
- [16] S. Fan and C. Frueh, “Multi-hypothesis light curve inversion scheme for convex objects with minimal observations,” in *Proceedings of the 8th European Conference on Space Debris*, ESA Space Debris Office, 2021, pp. 1–7.
- [17] A. M. Friedman and C. Frueh, “Observability of light curve inversion for shape and feature determination exemplified by a case analysis,” *Journal of the Astronautical Sciences*, vol. 69, no. 2, pp. 537–569, Apr. 2022. DOI: [10.1007/s40295-021-00293-w](https://doi.org/10.1007/s40295-021-00293-w).

- [18] R. Linares, M. Jah, and J. Crassidis, “Inactive space object shape estimation via astrometric and photometric data fusion,” *Advances in the Astronautical Sciences*, vol. 143, pp. 217–232, Jan. 2012.
- [19] R. Linares, M. K. Jah, J. L. Crassidis, and C. K. Nebelecky, “Space object shape characterization and tracking using light curve and angles data,” *Journal of Guidance, Control, and Dynamics*, vol. 37, no. 1, pp. 13–25, 2014. DOI: [10.2514/1.62986](https://doi.org/10.2514/1.62986).
- [20] R. Linares and R. Furfaro, “Space object classification using deep convolutional neural networks,” in *19th International Conference on Information Fusion*, Jul. 2016, pp. 1–8.
- [21] E. Kerr, G. P. Elisabeth, P. Talon, and D. Petit, “Using ai to analyse light curves for geo object characterisation,” in *Proceedings of the 22nd Advanced Maui Optical and Space Surveillance Technologies Conference*, 2021, pp. 1–9.
- [22] D. Hall, B. Calef, K. Knox, M. Bolden, and P. Kervin, “Separating attitude and shape effects for non-resolved objects,” in *The 2007 AMOS Technical Conference Proceedings*, Maui Economic Development Board, Inc. Kihei, Maui, HI, 2007, pp. 464–475.
- [23] D. O. Fulcoy, K. I. Kalamaroff, and F. K. Chun, “Determining basic satellite shape from photometric light curves,” *Journal of Spacecraft and Rockets*, vol. 49, pp. 76–82, 2012.
- [24] T. Yanagisawa and H. Kurosaki, “Shape and motion estimate of leo debris using light curves,” *Advances in Space Research*, vol. 50, no. 1, pp. 136–145, 2012, ISSN: 0273-1177. DOI: <https://doi.org/10.1016/j.asr.2012.03.021>.
- [25] D. Kobayashi and C. Frueh, “Compressed sensing for satellite characterization: Shadowing as a sensing matrix,” *8th European Conference on Space Debris*, vol. 8, Apr. 2021. DOI: [10.13140/RG.2.2.30685.33765](https://doi.org/10.13140/RG.2.2.30685.33765).
- [26] J. urech and M. Kaasalainen, “Photometric signatures of highly nonconvex and binary asteroids,” *Astronomy & Astrophysics*, vol. 404, no. 2, pp. 709–714, Jun. 2003. DOI: [10.1051/0004-6361:20030505](https://doi.org/10.1051/0004-6361:20030505).
- [27] M. Viikinkoski, J. Hanu, M. Kaasalainen, F. Marchis, and J. urech, “Adaptive optics and lightcurve data of asteroids: twenty shape models and information content analysis,” *Astronomy and Astrophysics*, vol. 607, pp. 1–14, Nov. 2017. DOI: [10.1051/0004-6361/201731456](https://doi.org/10.1051/0004-6361/201731456).

- [28] K. Ikeuchi, “Recognition of 3-d objects using the extended gaussian image.,” in *IJCAI*, 1981, pp. 595–600.
- [29] J. J. Little, “Extended gaussian images, mixed volumes, shape reconstruction,” in *Proceedings of the First Annual Symposium on Computational Geometry*, ser. SCG ’85, Baltimore, Maryland, USA: Association for Computing Machinery, 1985, pp. 15–23, ISBN: 0897911636. DOI: [10.1145/323233.323236](https://doi.org/10.1145/323233.323236). [Online]. Available: <https://doi.org/10.1145/323233.323236>.
- [30] B. Nicolet, A. Jacobson, and W. Jakob, “Large steps in inverse rendering of geometry,” *ACM Transactions on Graphics (Proceedings of SIGGRAPH Asia)*, vol. 40, no. 6, Dec. 2021. DOI: [10.1145/3478513.3480501](https://doi.org/10.1145/3478513.3480501).
- [31] C. Früh and M. K. Jah, “Coupled orbit attitude motion of high area-to-mass ratio (hamr) objects including efficient self-shadowing,” *Acta Astronautica*, vol. 95, pp. 227–241, 2014, ISSN: 0094-5765. DOI: <https://doi.org/10.1016/j.actaastro.2013.11.017>.
- [32] M. D. Shuster, “Survey of attitude representations,” *Journal of the Astronautical Sciences*, vol. 41, no. 4, pp. 439–517, Oct. 1993.
- [33] B. Duvenhage, K. Bouatouch, and D. Kourie, “Numerical verification of bidirectional reflectance distribution functions for physical plausibility,” in *SAICSIT ’13: Proceedings of the South African Institute for Computer Scientists and Information Technologists Conference*, Oct. 2013, pp. 200–208, ISBN: 9781450321129. DOI: [10.1145/2513456.2513499](https://doi.org/10.1145/2513456.2513499).
- [34] D. Newell and E. Tiesinga, *The international system of units (si), 2019 edition*, en, 2019-08-20 2019. DOI: <https://doi.org/10.6028/NIST.SP.330-2019>.
- [35] H. Krag, “A method for the validation of space debris models and for the analysis and planning of radar and optical surveys,” Ph.D. dissertation, Technische Universität Braunschweig, Mar. 2003.
- [36] C. Frueh, *Space traffic management*, Lecture Notes, 2019.
- [37] F. Falchi, P. Cinzano, D. Duriscoe, *et al.*, *Supplement to: The new world atlas of artificial night sky brightness. v. 1.1. gfz data services*. <https://doi.org/10.5880/GFZ.1.4.2016.001>, Accessed: 2023-08-25, 2016.

- [38] A. e. a. Vallenari, “Gaia Data Release 3. Summary of the content and survey properties,” *Astronomy & Astrophysics*, vol. 674, A1, A1, Jun. 2023. DOI: [10.1051/0004-6361/202243940](https://doi.org/10.1051/0004-6361/202243940). arXiv: [2208.00211](https://arxiv.org/abs/2208.00211) [[astro-ph.GA](#)].
- [39] J. C. Segovia, *Astroquery.gaia package*, <https://astroquery.readthedocs.io/en/latest/gaia/gaia.html>, Accessed: 2023-08-21, 2016.